ACS APPLIED ENERGY MATERIALS

www.acsaem.org Article

Properties of HPT-Processed Large Bulks of p-Type Skutterudite $DD_{0.7}Fe_3CoSb_{12}$ with ZT > 1.3

Gerda Rogl,* Oliver Renk, Sanyukta Ghosh, Ramesh Chandra Mallik, Andriy Grytsiv, Jiri Bursik, Erhard Schafler, Filip Tuomisto, Ernst Bauer, and Peter Franz Rogl

Cite This: *ACS Appl. Energy Mater.* 2021, 4, 4831−4844 Read Online

ACCESS | Metrics & More | Article Recommendations | Supporting Information

ABSTRACT: The influence of shear strain on the microstructural, physical, and mechanical properties was studied on large bulk samples (diameter: 30 mm, thickness: 1 or 8 mm), which were consolidated by high-pressure torsion (HPT) from a commercial powder $DD_{0.7}Fe_3CoSb_{12}$. Particularly, the thick sample (mass ∼ 53 g) allowed measuring the thermoelectric (TE) properties with respect to various orientations of the specimen in the sample. All data were compared with those of a hot-pressed (HP) reference sample, prepared with the same powder. Transmission electron microscopy, as well as X-ray powder diffraction profile analyses, Hall measurements, and positron annihilation spectroscopy, supported these investigations. Furthermore, synchrotron data for the temperature range from 300 to 825 K were used to evaluate the changes in the grain size and dislocation density as well as the thermal expansion coefficient via the change in the lattice parameter during heating. In addition, hardness and direct thermal expansion measurements of the HPT samples were performed and compared with the HP reference sample's values. With the increase of the shear strain from the center to the rim of the sample, the electrical resistivity becomes higher, whereas the thermal conductivity becomes lower, but the Seebeck coefficient remained almost unchanged. For the thin as well as thick samples, the enhanced electrical resistivity was balanced out by a decreased thermal conductivity such that the maximum ZT values (ZT = 1.3−1.35 at 856 K) do not vary much as a function of the shear strain throughout the sample, however, all ZTs are higher than that of the HP sample. The thermal−electric conversion efficiencies are in the range of 14−15% (for 423−823 K). With similar high ZT values for the n-type skutterudites, fabricated in the same fast and sustainable way, these p- and n-type skutterudites may serve as legs for TE generators, directly cut from the big HPT bulks.

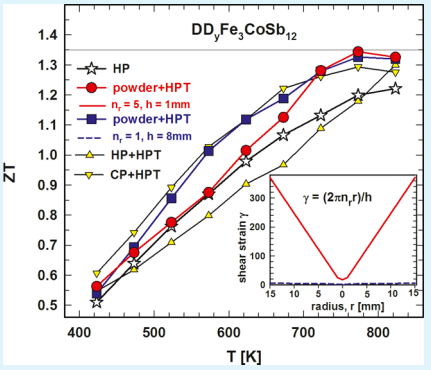

KEYWORDS: *skutterudites, thermoelectrics, nanostructures, high-pressure torsion, severe plastic deformation*

1. INTRODUCTION

Thermoelectricity is a simple and green technology for the direct conversion of heat (i.e., any exhaust heat, geothermal, solar heat, or even body heat) into electricity, and vice versa. For such a thermoelectric (TE) device (i.e., a TE generator), p- and n-type legs are needed, which are connected thermally in parallel and electrically in series. The quality of a TE material is judged by the dimensionless figure of merit $ZT = S^2T/\rho\lambda$, where S is the Seebeck coefficient, T is the absolute temperature, ρ is the electrical resistivity, and λ is the thermal conductivity, consisting of the lattice and carrier conductivity ($\lambda = \lambda_{ph} + \lambda_e$), as well as by the so-called thermal−electric conversion efficiency

$$\eta = \frac{T_h - T_c}{T_h} \frac{\sqrt{1 + (ZT)_a} - 1}{\sqrt{1 + (ZT)_a} + \frac{T_c}{T_h}} \quad (1)$$

including the Carnot efficiency, where T_h and T_c are the temperatures on the hot and cold sides of a TE generator, respectively, and $(ZT)_a$ is the average ZT over the temperature range applied. Therefore, an ideal TE material should simultaneously possess a high Seebeck coefficient, such as a semiconductor or a semimetal, a low electrical resistivity as well as a low thermal conductivity such as a metal and a glass, respectively, and all that within the temperature gradient applied.

Among the wide spectrum of TE materials, like half-Heusler alloys, tellurides, silicides, selenides, or Zintl phases,[1−17] p- and n-type skutterudites have been proven to have excellent high ZT values and efficiencies,[18−28] but still it is the goal of researchers to further improve them. One among various possibilities to further enhance ZT and η is to decrease the grain size and introduce defects and other crystal imperfections such as dislocations to enhance phonon boundary scattering at interfaces and consequently to reduce the lattice thermal

Received: February 8, 2021
Accepted: March 15, 2021
Published: April 28, 2021

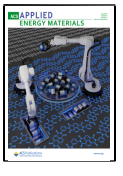

conductivity λ_{ph}.[29−32] This can be achieved by applying severe plastic deformation (SPD) via high-pressure torsion (HPT). With this technique severe torsional strain, increasing along the disc radius, is introduced, resulting not only in ultrafine or even nanocrystalline materials but also in a high density of crystal lattice defects, especially dislocations and grain boundaries with high angles of misorientation (ref 33 and references therein). The authors recently published an overview of the effects of SPD on the TE performance of skutterudites and Heusler and half-Heusler alloys, as well as of Bi-tellurides.[34]

In the case of ball-milled (BM) and hot-pressed (HP) unfilled,[35,36] single-,[37] double-, and multifilled[33,39,40] Sb-based skutterudites, after optimizing the processing parameters,[41] the authors could substantially enhance ZT (p-type: to ZT of 1.5;[42] n-type: to ZT of almost 2[23]) due to a significantly reduced thermal conductivity after HPT; however, the electrical resistivity was higher, and the Seebeck coefficient remained almost unchanged.

With the knowledge of the proper processing parameters (optimized number of revolutions, applied pressure, and processing temperature) of our previous investigations,[35−42] we tried as a further step to consolidate directly and plastically deform (HPT process) commercial p-type, $DD_{0.7}Fe_3CoSb_{12}$, and n-type, $(Sm,Mm)_{0.15}Co_4Sb_{12}$, skutterudite powder from cold-pressed (CP) powder pellets with a diameter of 10 mm and a thickness of less than 1 mm. ZTs ∼ 1.3 at 783 K and ZT ∼ 1.44 at 823 K, respectively, were achieved.[43,44] This method is time- and energy-saving, because ball milling and hot-pressing can be avoided, and the whole preparation method takes less than half an hour; however, for commercial use, these discs are rather small.

Recently, upscaling of HPT devices already allowed us to prepare n-type $(Sm,Mm)_{0.14}Co_4Sb_{12}$ skutterudite samples with a diameter of 30 mm and heights of about 1 mm and 8 mm starting from commercial powder. Depending on the shear strain introduced, that is, the position of the measured specimen in the large HPT disc, ZTs between 0.9 and ∼2.1 were achieved for the samples with a 1 mm thickness.[45] As a first success, a big sample with a thickness of 8 mm and a mass of ∼53 g was HPT-consolidated, revealing an almost homogeneous shear strain and ZTs between 1 and 1.4,[46] leading to the current work, that is, transferring this knowledge to p-type skutterudites.

For the present investigation, the HPT process is employed at 300 °C on p-type skutterudite powder, $DD_{0.7}Fe_3CoSb_{12}$, to produce for the first time large samples with a 30 mm diameter and thicknesses of about 1 and 8 mm. As HPT-processed samples inherently contain a gradient of the applied shear strain along the disc radius, all measurements need to be performed position-sensitive to reveal the influence of strain. Thus, because of the large radius of the samples, the larger strain gradient in the case of thin samples allowed studying the influence of shear strain on various properties measured, and comparing the strain−physical property behavior with that of the n-type skutterudite. In contrast to the thin samples, the marginal strain gradient in the case of thick HPT discs was utilized to compare the properties of specimens cut parallel and perpendicular to the rotation axis. It appears that ZTs are all higher than the ZT of the HP reference sample.

Transmission electron microscopy (TEM), as well as X-ray powder diffraction (XRD) profile analyses, synchrotron measurements, positron annihilation spectroscopy, and Hall measurements, complemented our investigation. In addition, hardness and thermal expansion measurements were performed and discussed.

2. EXPERIMENTAL SECTION

A total of five samples, s1, s2, s3, and s4, as well as the reference sample (referred to as HP), were prepared from the same batch of commercially sythesized p-type skutterudite powder (Treibacher Industry AG, Austria) with the nominal composition $DD_{0.7}Fe_3CoSb_{12}$ (DD stands for didymium, a natural rare earth double filler consisting of ∼95% of Nd and ∼5% of Pr). About 50% of the particles of the starting powder were smaller than 11 μm and 90% smaller than 27 μm. The reference sample, HP, prepared from 5 g of the powder, was hot-pressed (equipment: HP W 200/250 2200-200-KS) under an Ar atmosphere at a temperature of 700 °C and a pressure of 56 MPa.

The samples s1 to s4 were directly consolidated in a custom-built HPT device (Klement, Austria) at the Erich Schmid Institute in Leoben, Austria, using anvils with a diameter of 30 mm. An induction heating system from IEW corporation, attached to the HPT device, was used to heat the anvils and the powders to the desired temperature. To avoid loss of any powder, it was filled to top of a copper ring (hollow cylinder, wall-thickness 1 mm) as shown in Figure 1a, which was placed on the lower anvil (for the mass of

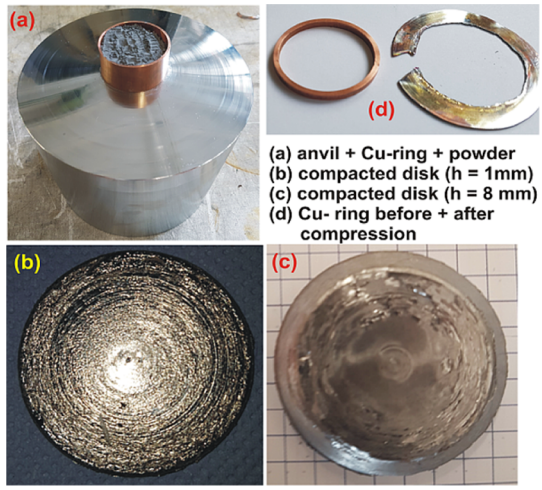

Figure 1. (a) Anvil plus copper ring, filled with powder, (b) sample s2 after HPT, (c) large sample s4 after HPT, and (d) copper ring with a 2 mm height before and after compression.

powder and dimensions of the respective ring, see Table 1). During prepressing under a nominal pressure of 5 GPa, the copper ring broke and fell off (see Figure 1d). Subsequently, the sample was heated to a processing temperature of 300 °C. Once the temperature was reached, the sample was kept for about 15 min at this temperature prior to deformation. HPT deformation was conducted under a nominal pressure of 5 GPa at a rotational speed of 0.2 rpm for five revolutions, that is, the entire preparation process was performed in less than 50 min.

For sample s1, a copper ring with a diameter of 30 mm and a height of only 2 mm was used. Due to the smaller amount of powder, the anvils came into contact with each other after 0.13 revolutions and the deformation process was stopped. Samples s2 (Figure 1b) and s3 were prepared with a higher (3 mm) copper ring and processing for five turns was successful (Table 1). For sample s4 (Figure 1a,c), one revolution was applied. As we already knew from the n-type material that the ZTs in the big sample with a height of 8 mm are almost alike, we wanted to save even more preparation time and energy by applying one revolution only and find out, how this low shear strain influences the respective properties.

All XRD data were collected using a Huber Guinier powder camera with an image plate recording system and monochromatic Cu Kα_1 radiation (λ = 0.154056 nm). Lattice parameters were calculated by

https://doi.org/10.1021/acsaem.1c00409
ACS Appl. Energy Mater. 2021, 4, 4831−4844

Table 1. Samples (s1, s2, s3, and s4); Height of the Copper Ring, h_{Cu}, in mm; Height of the Processed Sample, h_s, in mm; Mass of the Sample, m_s, in g; Number of Revolutions, n_r; Relative Density of the Whole Sample after Compaction, d_{rel}, in % (Error: 1%); Maximum Shear Strain, γ_{max}; and Shear Strain (Error: about 5%) in the Center of the Specimen Depending on the Specimen's Position, γ_I, I = A, B, C, D, a, b, c, d (for Details, See Figure 2)[a]

sample	h_{Cu}	h_s	m_s	n_r	D_{rel}	γ_{max}	γ_A	γ_B	γ_C	γ_D	γ_a	γ_b	γ_c	γ_d
s1	2.0	1.09	5.94	0.13	99.2	11	1.5		6.7				6.7	
s2	3.0	1.27	6.93	5	98.4	370			223		49			
s3	3.0	1.25	6.82	5	98.4	377	50	138	226	314		138	226	314
s4‖	16	8.0	55.04	1	96.4	11.8	3.4	5.4	6.7	8.8	3.4	5.4	6.7	8.8
s4=	16	8.0	55.04	1	96.4	11.8	3.4	3.1	5.3	7.8		3.1	5.3	7.8

[a]All copper rings had an inner diameter of 30 mm; all samples were deformed with an applied pressure of 5 GPa at a rotational speed of 0.2 rpm at a temperature T = 300 (±10 °C).

least-squares fits to the indexed 2θ values, calibrated with respect to Ge as internal standard (a_{Ge} = 0.565791 nm at room temperature) using the program STRUKTUR;[47] these data were double-checked employing a Rietveld refinement (program FULLPROF[48]), with which also the filling levels in site 2a of the skutterudite structure were determined.

Synchrotron radiation powder diffraction (SXRD) data were collected at the Taiwan Photon Source beam line (NSRRC, BM09A, λ = 0.61963 nm) at the National Synchrotron Radiation Research Center employing an ID IU22 crystal monochromator DCM with Si(111), an APD scintillation counter, a photodiode, PILATUS 200K, and a MYTHEN 24K, multicrystal analyzer. Measurements were performed with increasing temperature from 50 to 600 °C in steps of 50 °C. The XRD and synchrotron patterns were used to evaluate the crystallite size and its distribution as well as the dislocation density, applying the modified Williamson–Hall method developed by Ungar et al.,[49] using the convolutional multiple whole profile-fitting algorithm (CMWP). For details on these methods, see refs.[49−52]

Scanning electron microscopy (SEM) investigations on samples, broken to get a rough surface, were performed with a Tescan LYRA 3 XMU FEG/SEMxFIB instrument operated at 20 kV. A focused ion beam (FIB) workstation was used to prepare electron transparent thin lamellae of the samples from fracture surfaces. These lamellae were studied using a transmission electron microscope (Philips CM12 STEM, thermo-emission source 120 kV) and high-resolution transmission electron microscope (JEOL JEM-2100F, with a FEG and an accelerating voltage of 200 kV). The total length of dislocation segments visible in the TEM micrograph was measured either directly or by the line intersection method (LIM) and divided by the observed volume, for which the foil thickness was estimated as 30 nm. The LIM was applied to calculate the dislocation density.

For positron lifetime experiments, the samples were measured with a standard digital spectrometer with a time resolution of 250 ps (full width at half-maximum), using a ^{22}Na positron source wrapped in a 3 μm aluminum foil. 2 × 10^6 counts were collected in the lifetime spectrum for each of the samples studied. The aluminum foil caused a source correction of 210 ps (14.6% intensity) and the 1500 ps positronium correction varied between 0.0 and 0.12% (for more information, see ref 53).

The density, d_m, of the HP sample and the HPT-deformed samples s1−s4 as well as of various specimens cut from these samples was quantified using Archimedes' principle (error < 1%). The relative density, $d_{rel} = (d_m/d_X) \times 100$ (in %), was calculated with d_m and with the X-ray density, $d_X = (ZM)/(NV)$, where M is the molar mass, Z is the number of formula units per cell, N is Loschmidt's number, and V is the volume of the unit cell (see Table 1).

For measuring physical properties, the samples had to be cut into prisms (about 1 × 2 × 8 mm^3) for the measurement of the electrical resistivity and the Seebeck coefficient and into discs (about 1 mm height, 6 mm diameter) for measuring the thermal conductivity. The prisms and discs, used for measuring the transport properties, were cut from various places of the respective HPT disc. Specimens, cut for electrical resistivity and Seebeck measurements, are labeled as A, B, C, and D, depending on their position in the sample. Similarly, small letters a, b, c, and d are used for the specimens for thermal conductivity measurements (see insets in Figure 2). It should be noted that the positions of the specimens, shown in Figure 2, are only sketches and, therefore, are not completely true to scale. To avoid annihilation of any defects, the sample cutting and preparation were performed at room temperature, using superglue on the respective metal support for cutting.

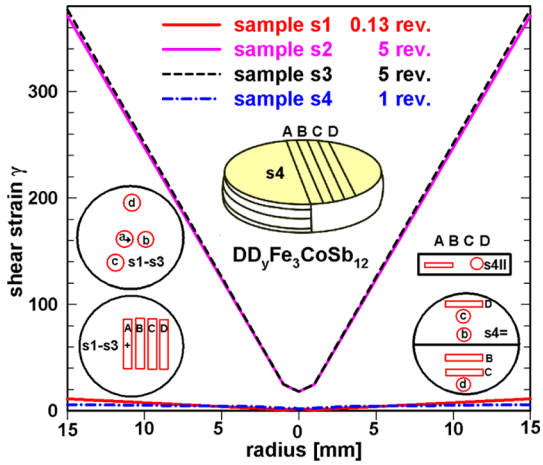

Figure 2. Shear strain of samples s1−s4 versus sample's radius for $DD_{0.7}Fe_3CoSb_{12}$. Insets: sketches of the processed discs (s1−s3) and slices (s4) with positions of the cut cuboids (A−D) and small discs (a−d).

As the shear strain, $\gamma = (2\pi n_r r)/h$ (n_r is the number of revolutions, r is the radius, and h is the thickness of the sample), increases from the center to the rim (Figure 2), the shear strain of each extracted specimen (i.e., discs and prisms) needs to be calculated individually. To arrive at reliable ZT values, it was ensured that the shear strain at the center of each cuboid matches with the shear strain at the center of the respective disc, which emphasizes that specimens with corresponding applied shear strain were paired, for example, A with a, B with b, and so on.

Due to fine cracks forming especially in the highly strained rim area, it was not always easy to prepare a crack-free prism and a disc-shaped specimen, both matching the same shear strain.

For measurements of electrical resistivity, ρ, and Seebeck coefficient, S, in the range of RT to 823 K, a ZEM-3 equipment (ULVAC-Riko, Japan) was employed (for details, see ref 23). These measurements were carried out twice, each time upon increasing and decreasing the temperature, but as it turned out that the second measurement was practically identical to the first one, the data of the second run are not shown here. Besides, to confirm our data, for a selected specimen (C of sample s2), ρ and S were measured in the temperature range of 373 to 773 K using a LINSEIS LSR-3 system in the Thermoelectric Materials and Devices Laboratory, Department of

https://doi.org/10.1021/acsaem.1c00409
ACS Appl. Energy Mater. 2021, 4, 4831−4844

Physics, of the Indian Institute of Science. For the measurement of the thermal conductivity, λ, a flash method (Flashline 300, ANTER, USA) was used, and measurements were performed at least twice with increasing temperature as discussed in ref 23. The temperature-dependent Lorenz number was calculated as proposed by Kim et al.[54] and served to derive λ_e, which was applied to calculate the phonon part of the thermal conductivity, λ_{ph}, using $\lambda = \lambda_e + \lambda_{ph}$. These measurements usually exhibit errors of about 5% (ρ and S) and 8% (λ). For the Hall measurement, a thin piece of about 0.4 mm thickness was contacted with four copper wires, which were connected with a Van-der-Pauw equipment, recently built and tested at TU Wien, Austria. The measurement was performed under a pressure of 5.4×10^{-6} mbar at temperatures from 297.5−520 K, applying magnetic fields from 0−10 T.

A microhardness tester, AD PAAR-MHT-4, mounted within a Zeiss Axioplan optical microscope was used to measure the static hardness on the surface of polished samples. Vickers hardness values were calculated according to HV = 1.891 $F/(2l)^2$ (F = 1 N is the load and $2l$ is the diagonal length of the indent). To get a constant average value and the respective error bar, at least 10 indents were collected.

The LINSEIS L75 Platinum Series equipment was applied to determine the thermal expansion from RT to 550 °C of s4 and the HP reference samples. These experimentally gained thermal expansion coefficients were compared with those evaluated from the change of the lattice parameter derived from synchrotron measurements.

In order to guide the reader easily through the text, the following terminology was applied: "sxpy", where s stands for sample, x gives the number of the sample, p the position of the measured specimen (A−D and a−d, see the inset in Figure 2), and y the number of the measurement run. Throughout the manuscript, in all figures, the reference HP sample is depicted with open symbols, the thermally stable (i.e., already annealed) samples with filled symbols.

3. RESULTS AND DISCUSSION

The shear strain was calculated for all specimens from the center of the sample (disc) to the center of the prism or little disc (Table 1). The specimens themselves are not perfectly homogeneous with respect to shear strain, but for samples s2 and s3, the shear strain hardly varies along the specimens' length or width (A−D) or along the diameter (a−d) (see Figure 2). As sample s1 was processed with 0.13 revolutions only and sample s4 has a height of 8 mm, the shear strain for these two samples was very low (see Figure 2 and Table 1). Therefore, one has not to worry about any strain inhomogeneity within the extracted specimens.

3.1. Microstructural Properties and Density. The normalized XRD profiles of $DD_{0.7}Fe_3CoSb_{12}$ as powder, HP, and HPT-compressed, showed minor amounts of secondary phases (<2 vol %); however, all half-widths of the HPT-processed samples are broader in comparison to the powder or the HP profile [Figure 3, enlarged peak (321)]. This peak broadening originates from the smaller grain sizes as well as from various defects, for example, dislocations, introduced during processing. Also, the peak broadening increases slightly from the center (specimen A) to the rim (specimen D), as the shear strain radially increases (see also Figure 2). Measurement-induced heating from room temperature to 823 K infers grain growth and annealing out of defects and as a consequence reduces the half widths slightly, though they still remain broader than those of the HP sample (Figure 3). From synchrotron radiation patterns (Figure 4), one can see that with increasing temperature the peak maxima are shifted to lower 2θ values and the peaks become slimmer, indicating growing lattice parameters and grain growth, respectively.

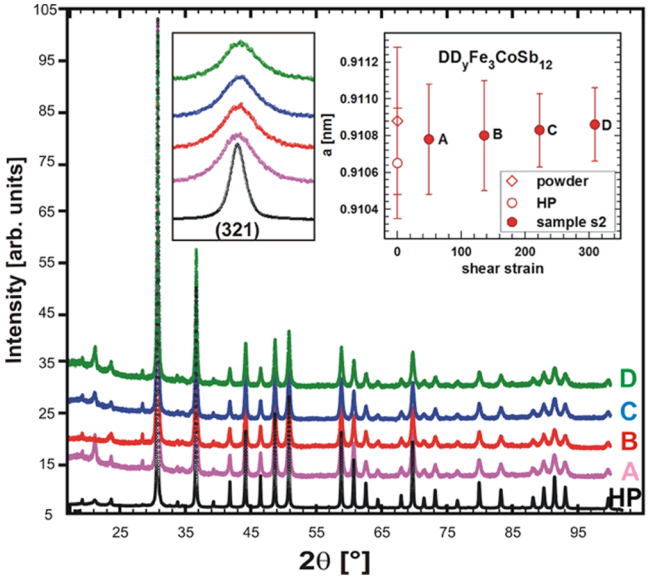

Figure 3. X-ray profile of $DD_{0.7}Fe_3CoSb_{12}$ (HP and from sample s2 specimens A to D): peak (321) enlarged. Inset: lattice parameters of the starting powder, HP, and A to D of s2.

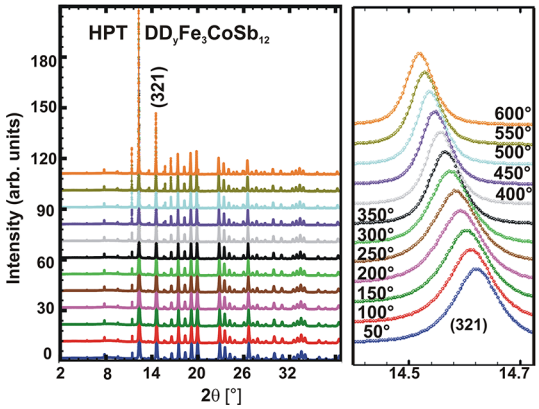

Figure 4. Synchrotron profiles of $DD_{0.7}Fe_3CoSb_{12}$ (s2A). Left panel: profiles for T = 50° C (323 K) to T = 600° C (873 K); right panel: peak (321) enlarged.

These features are especially well to be seen at the enlarged (321) peak (the right panel in Figure 4).

The filling level, y, of the reference sample, as well as of the HPT-processed samples, hardly changed and stayed at $y \sim 0.7$ (values derived from Rietveld refinement).

Due to severe strains applied, in some parts of the HPT discs, large cracks are obvious. Figure 5 displays the SEM images of fracture surfaces of samples s1 and s2, each of them taken at two different magnifications. In all cases, after annealing, the surface does not look as rough as before annealing; in addition, bigger grains are visible. Comparing the two annealed samples s1 and s2, one finds smaller grains in the case of s2. Also, the rim piece of s2 exhibits smaller grains than the center piece and overall, a more homogeneous structure, in line with the significantly larger shear strains applied.

Figure 6 gives detailed insights into the structure of the samples. The center part of sample s1 displays a heavily deformed microstructure with subgrains from 10 nm to several hundreds of nanometers, bigger sheared grains as well as cracks and dislocation walls. After annealing, the dislocation density at

https://doi.org/10.1021/acsaem.1c00409
ACS Appl. Energy Mater. 2021, 4, 4831−4844

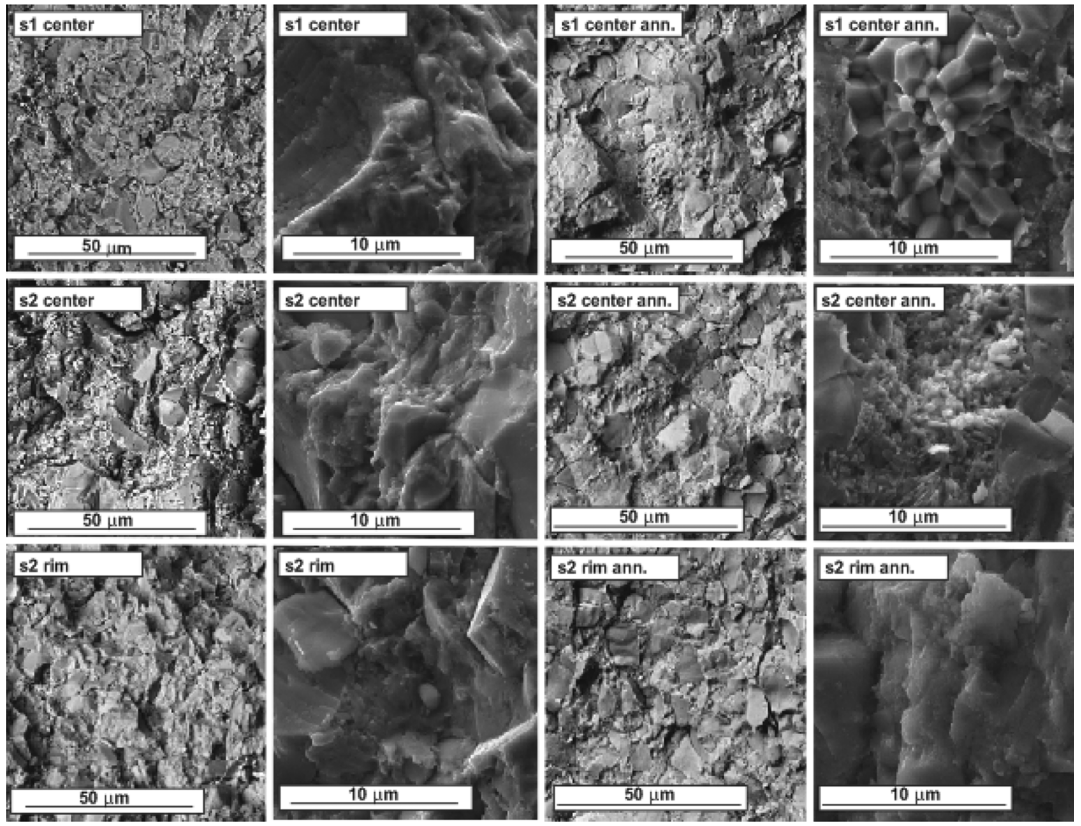

Figure 5. SEM images of fractured surfaces $DD_{0.7}Fe_3CoSb_{12}$ from samples s1 and s2 before and after annealing.

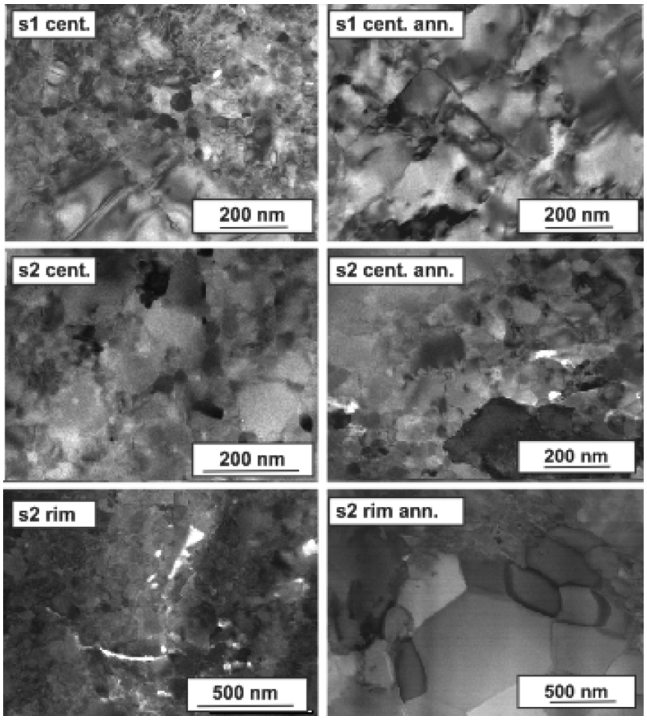

Figure 6. TEM images of samples s1 and s2 of $DD_{0.7}Fe_3CoSb_{12}$ taken near the center and at the edge of the HPT disc before and after annealing.

the center is nonuniform and lower. The annealed rim piece shows a partially recrystallized microstructure; there are regions with grown equiaxed grains free of dislocations next to nonrecrystallized areas with dislocations, which are not completely annealed out; therefore, the dislocation density is nonuniform.

The lattice parameter (Figure 7a) of the HP sample is slightly smaller than that of the powder and, taking the error bars into account, the lattice parameters of samples s1 to s4 are in the same range, though those of samples s2, s3, and s4 can be considered as slightly higher. The lattice parameters of the HPT samples are slightly smaller at the center than at the rim, which was confirmed with the evaluation of the lattice parameters of specimens A to D of sample s2 (inset in Figure 3). Generally, a small decrease occurs after annealing. It is easy to conceive that hot-pressing removes some of the defects and dislocations in the ball-milled starting powder, thereby reducing the lattice parameter. In contrast, a rising shear strain increases the defect level again and with it the lattice parameter.

The relative density (Figure 7b), due to fine mini cracks and voids, is lower for HPT-consolidated samples than for the HP reference sample, in line with earlier findings.[21,38−46] Although the difference is marginal, the relative density is higher in the center of the samples than in the rim area due to more voids forming with higher shear strains. Heat treatments cause a slight densification. We observed such a behavior already in former investigations on smaller skutterudite specimens.[40,41,43−46,55]

For all samples, the dislocation density does not differ much among the various samples (Figure 7c). The dislocation density of the HP powder is more or less in the same range as the dislocation density in the center of the HPT-deformed samples. This relates to the fact that the plastic deformation at the center is theoretically zero, practically very low (extension

https://doi.org/10.1021/acsaem.1c00409
ACS Appl. Energy Mater. 2021, 4, 4831−4844

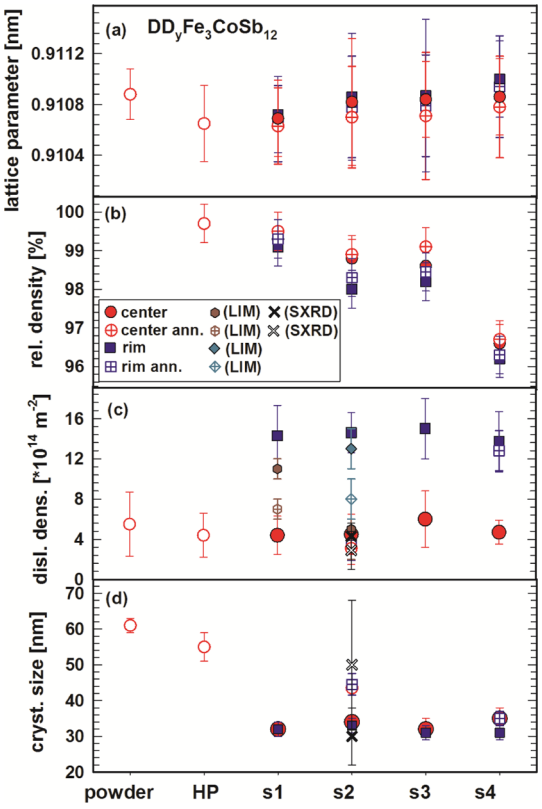

Figure 7. $DD_{0.7}Fe_3CoSb_{12}$ as powder, HP, and HPT samples s1−s4, at room temperature, from top to bottom: (a) lattice parameter, a, (b) relative density, d_{rel}, (c) dislocation density, d, and (d) crystallite size, cs.

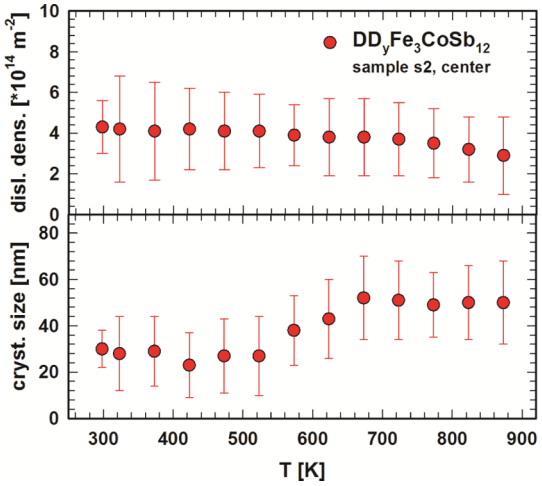

Figure 8. $DD_{0.7}Fe_3CoSb_{12}$, sample s2 center: dislocation density (upper panel) and crystallite size (lower panel) in dependence of temperature.

of the sample); however, the results from the outer rim of the sample are considerably higher by a factor of almost 3. Annealing slightly reduces the dislocation density, as shown for samples s1, s2, and s4.

Besides gaining the dislocation density from XRD as well as from SXRD (s2) patterns via the profile-fitting algorithm CMWP, for selected pieces, it was also calculated by the LIM from the TEM images. Figure 7c documents that generally both results are in a good agreement, although for sample s1 with LIM the dislocation density is higher than with the profile-fitting algorithm. The reason could be that for the LIM calculation a spot was selected, which was slightly off the center of the sample.

Naturally, the starting powder exhibits the largest crystallite size (Figure 7d) because of the enormous grain refinement, achieved by HPT; however, among the HPT samples, crystallite sizes do not differ much. Annealing induces grain growth, but even though, the crystallite sizes are still smaller than those of the HP reference sample and the powder.

Exemplarily for a center piece of sample s2, the SXRD data were evaluated by applying the Williamson−Hall method to gain the dislocation density and crystallite size for each measured temperature point (Figure 8). Whereas the dislocation density decreases almost linearly with increasing temperature, the crystallite size shows a stronger growth between 500 and 700 K before more or less balancing out above 700 K. The thus-obtained data are in good agreement with those extracted from the XRD patterns (compare Figures 7 and 8).

3.2. Temperature-Dependent Transport Properties.

Specimens for physical property measurements were deliberately cut from different positions of a sample, as the radius-dependent shear strain strongly affects the micro- and defect structure. A comparison of sample s1, subjected to only 0.13 revolutions, with the other 1 mm thick samples allows understanding the influence of the number of rotations on the physical properties. Samples s2 and s3 served to investigate the influence of the radial increase of shear strain from the center to the rim. As expected, due to almost the same shear strain applied (Table 1), these two samples can be treated as equal with respect to their thermal transport properties: the temperature-dependent electrical resistivity $\rho(T)$ and Seebeck coefficient $S(T)$ of s2C and s3C are the same within the error bar (see Figure S1 in Supporting Information). In addition, one can see that a second measurement with increasing and decreasing temperatures, performed with a different equipment in a different lab, confirms not only thermal stability after the first run, but also the accuracy of the original measurement.

The 8 mm thick sample, s4, allowed studying the differences in the physical properties along two directions: parallel and perpendicular to the HPT rotation axis.

3.2.1. Samples s1, s2, and s3. Although specimens s1C and s2C were cut from the same position in the two samples, one must consider that the shear strain of s2C is 33 times higher than that of s1C, which explains the quite different TE behavior.

The electrical resistivity, $\rho(T)$ (Figure 9a), of all four specimens of s2 is generally higher than $\rho(T)$ of the HP sample. In addition, the higher is the shear strain, the higher is $\rho(T)$, that is $\rho(T)$ of specimen D is about six times higher than that of specimen A. Generally, the $\rho(T)$ curve exhibits the same temperature dependence for all measured specimens, independent of the radial position (A to D). During heating (curves labeled with index 1), $\rho(T)$ increases with increasing temperature, showing a metal-like behavior, with an anomaly between 520 and 620 K, followed by a further very slight increase. This anomaly occurs at higher temperatures for higher shear strains. Such anomalies were also found for the small CP+HPT-processed p-type skutterudites[43,44] as well as for the HP+HPT samples [e.g., ref[39,40,42]] and can be explained with the annealing out of defects, mainly holes. As

https://doi.org/10.1021/acsaem.1c00409
ACS Appl. Energy Mater. 2021, 4, 4831−4844

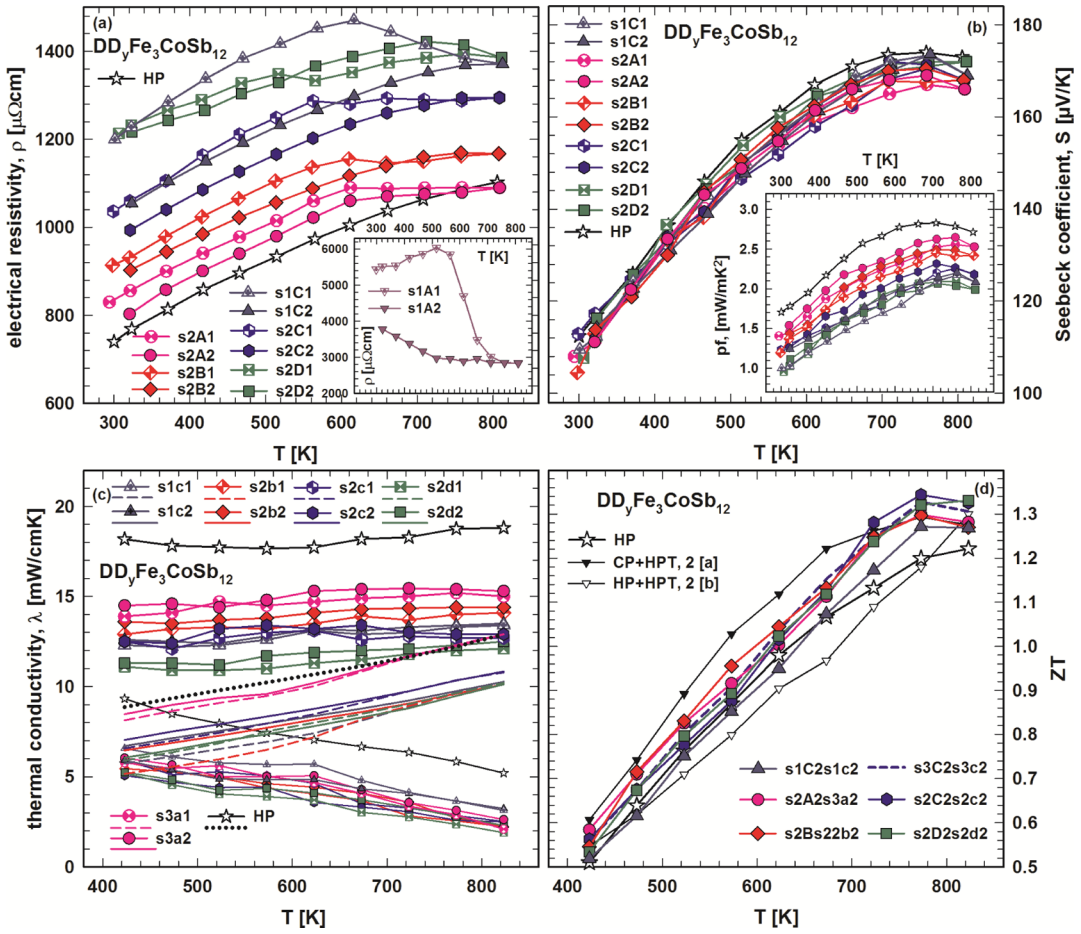

Figure 9. $DD_{0.7}Fe_3CoSb_{12}$: (a) electrical resistivity, ρ [inset: $\rho(T)$ of s1A1 and s1A2], (b) Seebeck coefficient, S (inset: power factor, pf), (c) thermal conductivity, λ, lattice thermal conductivity (small symbols), phonon part (λ_{ph}), and electronic part of the thermal conductivity, λ_e (lines without symbols), and (d) ZT versus temperature, T, of samples s1, s2, and s3 in comparison to the HP sample and in the case of ZT in comparison to a CP+HPT sample ([a] = [43]) and of a HP+HPT sample ([b] = [40]) from earlier works of the authors.

shown in Figure 8, this is the temperature range of strong grain growth. In this context, it is worth mentioning that this anomaly of $\rho(T)$ usually occurs at the same temperature at which in the case of thermal expansion measurements, a significant contraction takes place.[56]

For decreasing temperature, $\rho(T)$ of specimens B2, C2, and D2 (2 indicating the cooling cycle) does not show any anomalies. The $\rho(T)$ values are higher than those of the HP reference sample and decrease with decreasing temperature. Specimen A2 shows a slight anomaly between 650 and 850 K with resistivity values in the range of the HP sample.

Although the shear strain on specimen s1C is lower than on all specimens of s2 (Table 1), the electrical resistivity is the highest with a prominent hysteresis of $\rho(T)$ between the values measured for increasing and decreasing temperatures. The shape of the $\rho(T)$ curve for heating is the same as for the HP +HPT-processed samples,[39] that is $\rho(T)$ increases with increasing temperature and after a plateau-like maximum, $\rho(T)$ decreases, proving that the structure of this sample is typical for a HP+HPT sample. The grains seem not to be fused initially as well as in samples s2 or s3, thus causing such a high electrical resistivity in s1C; during the first heating, they fuse at around 600 K in parallel with annealing out of defects and holes. Specimen s1A was cut from the center part of sample s1, where the shear strain is almost zero (see Figure 2, Table 1). As depicted in the inset of Figure 9a, specimen s1A has an extremely high electrical resistivity with a maximum at 520 K and a change from metallic to semiconducting-like behavior. This specimen is excluded from the further physical property discussion, as due to the low strain, the grains in this specimen seem not to be fused together.

HPT processing has hardly any influence on the Seebeck coefficient (Figure 9b). Thus, all temperature-dependent Seebeck values, independent of the applied shear strain, are very close to each other, though the HP sample exhibits a little bit higher values above 550 K.

With the equation proposed by Goldsmid and Sharp[57]

$$S_{max} = E_g/(2eT_{max}) \quad (2)$$

where e is the elementary charge and T_{max} is the absolute temperature at which S_{max} occurs, the energy gap E_g of the electronic density of states in the proximity of the Fermi energy E_F was calculated. As S_{max} and T_{max} are about the same, similar energy gaps for all thermally stable specimens can be calculated. For sample s2, this yields $E_g \sim 245$ meV, while being slightly higher for s1C ($E_g \sim 265$ meV). All these values are in good agreement with those of the small CP- and HPT-compacted (CP+HPT) samples of our previous study,[43] with energy gaps in the range of 237−274 meV.

Figure 10 shows the charge carrier density (left panel) and the Hall mobility (right panel) for two selected specimens, one from the center area of sample s3 and one of sample s4 (piece

https://doi.org/10.1021/acsaem.1c00409
ACS Appl. Energy Mater. 2021, 4, 4831−4844

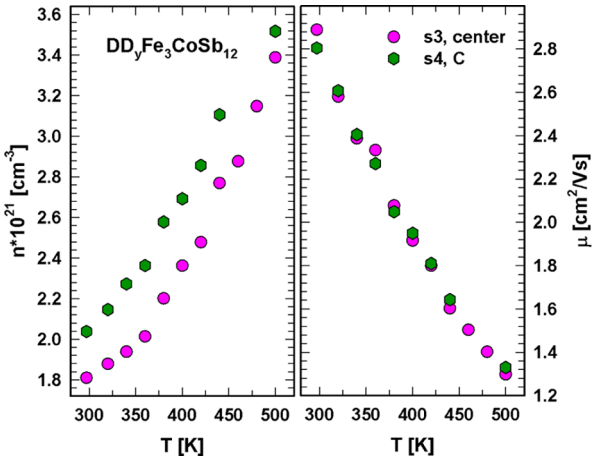

Figure 10. $DD_{0.7}Fe_3CoSb_{12}$: charge carrier density, n (left panel), and mobility, μ (right panel), as a function of temperature, T, of samples s3 center and s4 = C.

C, see Figure 2). The values obtained (for evaluation details, see the text and Figure S2 in the Supporting Information) do not differ much. While the number of charge carriers in the range of 300−500 K increases with increasing temperature, their mobility decreases. The charge carrier density of s3 is slightly lower than that of s4 (e.g., at room temperature $n = 1.8 \times 10^{21}$ cm^{-3} for s3 and $n = 2.0 \times 10^{21}$ cm^{-3} for s4) in accordance with a slightly higher Seebeck coefficient, and is in the range of the small CP+HPT sample.[43] Although there is a slight difference in the charge carrier density for samples s3 and s4 in the temperature range of 300−500 K, due to different resistivities, the mobility is almost alike, with a decrease from $\mu \sim 2.8$ cm^2/Vs to $\mu \sim 1.3$ cm^2/Vs in this temperature range. Due to a lower electrical resistivity, the mobility for the HP sample is slightly higher.

As the slopes of all $S(T)$ curves are almost alike and linear in the temperature range below 500 K, as a cross-check, the charge carrier concentration can be estimated from Mott's formula assuming that the effective electron mass m^* corresponds to the free electron mass

$$S = \frac{\pi^2 k_B{}^2 2m^*}{|e|\hbar^2(3n\pi^2)^{2/3}}T \qquad (3)$$

with k_B being the Boltzmann constant and $\hbar$ the reduced Planck's constant. In the range of 300−500 K, this estimation yields $n \sim 2.7 \times 10^{21}$ cm^{-3}, confirming the Hall data given above.

The power factor for all samples is shown in the inset of Figure 9b. All values are close to those of the HP reference sample, and due to almost the same Seebeck coefficient for all samples, the power factor is mainly governed by the electrical resistivity, that is the lower the electrical resistivity, the higher the power factor; therefore, the highest values are reached for the HP sample with 2.8 mW/mK^2 at 708 K. Among the HPT-consolidated samples, s2A2 with 2.6 mW/mK^2 at 756 K shows the highest value, reaching almost the one of the HP sample.

The temperature-dependent thermal conductivity with its electronic and phonon part is displayed in Figure 9c. Whereas λ_e increases with increasing temperature, λ_{ph} consequently decreases. The electrical resistivity generally increases from the center toward the rim, due to finer grains and an enhanced defect density, for the thermal conductivity, it is the opposite, decreasing with increasing shear strain, and within the measured range, λ is almost temperature-independent. For all specimens, the λ values are lower than those of the HP sample, which also applies to the lattice thermal conductivity. Due to grain growth, the values for the annealed specimens are slightly higher.

The temperature-dependent ZTs of the HP- and the HPT-processed samples as well as data from earlier findings of the authors[40,43] are depicted in Figure 9d. The thermally stable specimen C of sample s1 exhibits a ZT of almost 1.3 at 773 K, which is slightly higher than ZT = 1.2 of the HP sample at 810 K. This result shows that heating the powder to 300 °C under a pressure of 5 GPa for 15 min can already produce materials with at least the same ZT as after time- and energy-consuming hot-pressing (at 56 MPa). All ZTs of samples s2 and s3 are in the same range with ZTs around 1.3 reaching almost 1.4 at 773 K. ZT values do not vary much as a function of the shear strain because at an almost constant Seebeck coefficient, resistivities increase from the center to the rim but are balanced out by concomitantly decreasing thermal conductivities. This finding that ZT for all four p-type specimens does not vary too much is new; it is in contrast to the n-type skutterudites investigated in a recent work of the authors,[45] where ZT varied from about 1 to 2.1 (sample with a diameter 30 mm and a thickness of 1 mm, fabricated under the same conditions as sample s2). In

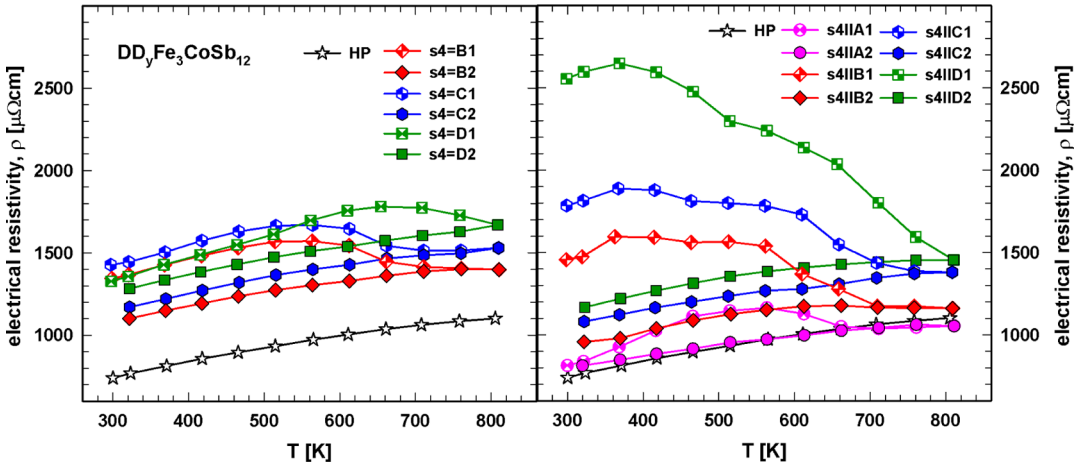

Figure 11. $DD_{0.7}Fe_3CoSb_{12}$: electrical resistivity, ρ, versus temperature, T, of sample s4= (left panel) and of sample s4|| (right panel).

https://doi.org/10.1021/acsaem.1c00409
ACS Appl. Energy Mater. 2021, 4, 4831−4844

addition, this may be taken as a confirmation that s2 and s3 with respect to physical properties can be treated as equal. All these ZT values are excellent for p-type skutterudites and are higher than that of the HP sample; furthermore, they are in the same range as those of the CP+HPT and the HP+HPT samples. The thermal−electric conversion efficiency, calculated with eq 1, is about $\eta_{423-823K}$ = 13.8% for the HP sample and s1C2, for all other HPT samples, $\eta_{423-823K}$ = 14.4−14.7% (for details, see Figure 13, Section 3.2.3.).

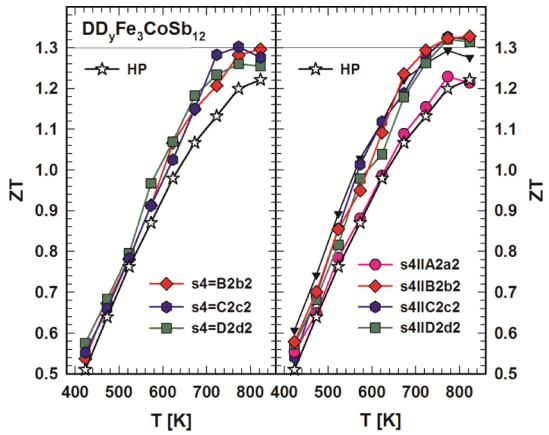

Figure 12. $DD_{0.7}Fe_3CoSb_{12}$: ZT versus temperature, T, of sample s4= (left panel) and of sample s4|| (right panel).

3.2.2. Sample s4. Sample s4 is 8 mm thick with a mass of ~53 g. Due to the thickness and the fact that s4 was HPT-consolidated within one turn, the variation of shear strain across the sample is low, allowing us to focus on the directional dependence of the TE properties. Accordingly, sample s4 was cut into slices perpendicular (s4=) and parallel (s4||) to the rotation axis, as shown in Figure 2.

Comparing the temperature-dependent behavior of the electrical resistivity (Figure 11) of specimens cut from these different sets of slices, one can immediately see that the shape of the respective $\rho(T)$ curves for the first measurement with increasing temperature is different for the specimens cut perpendicular and parallel to the rotational axis. Although the shear strain within the sample does not change much, it has an influence on the electrical resistivity.

All specimens from s4= (Figure 11, left panel) exhibit $\rho(T)$-curves similar to those of the thin samples, with the electrical resistivity increasing with increasing temperature till a maximum is reached, before decreasing at higher temperatures. This maximum is slightly shifted with increasing shear strain from 500 to 650 K, which means that for higher shear strain (s4=D) more defects, especially holes, are introduced, and the grains are smaller, and therefore it takes a higher temperature to anneal most of the defects out. In addition, $\rho(T)$ is shear-strain-dependent, increasing toward the rim of the HPT sample. For the first measurement with decreasing temperature and further measurements with heating and cooling (not shown), the $\rho(T)$-behavior is metal-like with curves almost in parallel to the HP $\rho(T)$ curve, though shifted to higher values.

Comparing these observations with the $\rho(T)$ curves of s4||, one can see (Figure 11, right panel) that during the first heating cycle, all specimens, except A, exhibit a maximum already at about 370 K and show a second slight anomaly between 500 and 600 K. In this context, it must be noted that

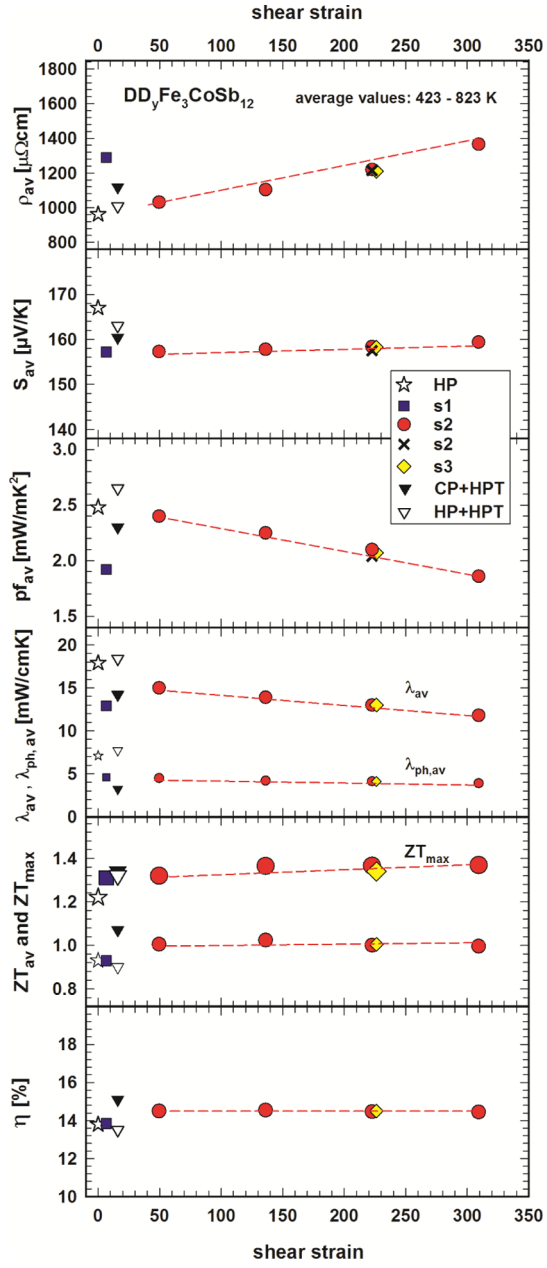

Figure 13. $DD_{0.7}Fe_3CoSb_{12}$, samples s1, s2, s3, HP, HP+HPT, and CP+HPT: average values (423−823K) from top to bottom of electrical resistivity, Seebeck coefficient, power factor, thermal conductivity, and lattice thermal conductivity (smaller symbols), ZT, and, in addition, ZT_{max} at 810 K (big symbols) and efficiency in dependence of shear strain. Note: all values are from the thermally stable measurements, the symbol × represents s2C4, measured with a different equipment. The lines are guides to the eye.

the shear strain of all specimens of s4= can be considered as homogeneous, whereas for the specimens of s4||, there is a gradient of shear strain within each specimen (see Figure 2). Obviously, because of the shear-inhomogeneity of these specimens, some of the introduced defects already annihilate at around 370 K while heating the specimen during the measurement. Still, higher temperatures are needed to anneal out almost all of them. For the cooling cycle, the $\rho(T)$ curves hardly differ from those of s4= in shape, but values are slightly lower.

https://doi.org/10.1021/acsaem.1c00409
ACS Appl. Energy Mater. 2021, 4, 4831−4844

For all specimens of s4= and s4||, the shape of all temperature-dependent Seebeck curves (displayed in Figure S3 of the Supporting Information) looks practically alike and is the same as for samples s1, s2, and s3 and in the range of or only slightly lower for the HPT-compacted sample compared to the HP one. The heating and cooling curves are almost identical.

The energy gap values, calculated with eq 2, do not vary much and are in the range of $E_g \sim 250$ meV, not differing much from that of the thin sample s2. The charge carrier density obtained from the calculation with eq 3 yields $n \sim 2.8 \times 10^{21}$ cm^{-3} for all specimens; the average charge carrier mobility, calculated with equation $\mu = 1/(\rho ne)$, gives $\mu \sim 2.1$ cm^2/Vs, data, which are in good agreement with those gained via Hall measurements performed for specimen C of s4=, shown in Figure 10.

The power factor, displayed in the inset of Figure S3 of Supporting Information, is generally lower for all specimens of s4= and s4|| than that of the reference HP sample. As the temperature-dependent power factors are governed mostly by the electrical resistivity, they are closer to each other for specimens A−D for s4= than for s4||. The highest power factor of this series of all thermally stable specimens has A2 of s4|| with 2.8 mW/mK^2 at 760 K, due to a very low electrical resistivity.

Thermal conductivity is practically temperature independent and lower than the thermal conductivity of the HP sample (see Figure S4 in Supporting Information). Sample s4||a displays the highest values, corresponding to the extremely low electrical resistivity. All phonon contributions of the thermal conductivity decrease with increasing temperature and reach very low values.

Except for s4||A2a2 with values in the range of the HP sample (ZT = 1.2 at 810 K), all other ZT values of the big sample s4 exceed those of the HP sample and are in the range of ZT = 1.3 above 800 K, independent of the position of the measured specimen (Figure 12). The thermal−electric conversion efficiency, η, reaches very good values with $\eta_{423-810K} = 14.5 \pm 0.3\%$. As s4 seems to be more or less homogeneous, with respect to ZT, it could be used to cut p-legs for TE modules directly. Recently, the authors have reported on the n-type counterpart, with ZTs in the same range as that for a big sample like s4.[46]

3.2.3. Comparison of TE Properties in Dependence of Shear Strain. Figure 13 clearly documents the practically linear dependence of the average values (T = 423−823 K) of the thermal transport properties on the shear strain. In addition, the highest ZT values and the efficiency (T = 423−823 K) are depicted. Before discussing the data, the reader should be reminded that sample s1 was HPT-processed with 0.13 revolutions only and contains a reduced gradient of shear strain, compared to samples s2 and s3. Furthermore, in Figure 13, the data of the HP, the HP+HPT,[40] and CP+HPT[43] samples as well as of s3C2 and of s2C4, the latter measured in another laboratory, are added for comparison.

For the four specimens of sample s2 (see Figure 13), the electrical resistivity increases with increasing shear strain from the center to the rim and so does, but only to a minor and practically negligible extent, the Seebeck coefficient. In contrast, the thermal conductivity as well as the lattice thermal conductivity decrease with increasing shear strain. Both effects arise from the fact that the grains become smaller and the defect density becomes higher with increasing strain toward the rim. As the Seebeck coefficient of all HPT-alloys does not change as a function of the shear strain and is within the error bar alike the one for the HP reference sample, one can exclude strong changes in the band structure and relative position of the Fermi-level; impurity states may develop but are without influence. Whereas the Seebeck values of all samples are very close to each other, the resistivity values are spread over a wider range. The power factor, usually mainly dependent on the Seebeck coefficient, is consequently in this investigation mainly governed by the electrical resistivity and decreases with increasing shear strain. Although the Seebeck value for sample s1 is in the range of that of s2, the electrical resistivity, due to lower density, is higher, resulting in a lower power factor.

It is important to point out that the data for specimen s3C2 perfectly agree with the results of the measurements of s2C2. Also, the resistivity and Seebeck data of s2C4, the thermally stable specimen, measured under different laboratory conditions fit perfectly well. Comparing these data with those of HP, CP+HPT,[43] and HP+HPT samples,[40] one can see that the data match quite well.

Thermal conductivity values of all HPT samples, independent of their production route, are lower than the thermal conductivity of the HP sample. Thermal conductivities and lattice thermal conductivities of all samples s2 and s3 decrease slightly with increasing shear strain, as expected because of the increasing resistivity. Sample s1 with the highest resistivity exhibits the lowest thermal conductivity.

All ZTs and average ZTs of the HPT samples are higher than those of the HP sample with ZT = 1.2 at 823 K. As lower thermal conductivities balanced out higher electrical resistivities and the Seebeck coefficients only changed negligibly, ZTs are more or less the same. For all specimens of s2, ZT is higher than 1.3, reaching almost 1.4, which is higher than ZT values for s1 and the CP+HPT and HP+HPT (ZT ∼ 1.3) samples.

All efficiencies of s2 and s3 are in the range of $\eta_{(423-823K)} \sim 14.6\%$. For sample s4, due to a very low strain variance, all average vales are very close to each other and, therefore, not shown in Figure 13. However, due to higher electrical resistivities, balanced out by low thermal conductivities and an almost unchanged Seebeck coefficient, the average ZT is rather homogeneous (ZT ∼ 1).

Positron annihilation spectroscopy is particularly suitable for studying vacancy-type defects in crystalline solids.[53] We compared the positron lifetime measured in the HP sample with those measured in samples HP+HPT and HP+HPT + annealed. The results are summarized in Table 2. The positron lifetime spectra could be decomposed to two exponential components, of which the shorter was 280−290 ps, dominating the spectra and the longer in the range 500−700 ps, with intensities in the range 1−6%. The average lifetime that coincides with the center of mass of the lifetime spectrum

Table 2. Positron Annihilation Data: Compound, Average Lifetime τ_{ave} in ps, τ_1 in ps, τ_2 in ps, and its Intensity I_2 in %[a]

$DD_{0.7}Fe_3CoSb_{12}$	τ_{ave}	τ_1	τ_2	I_2
HP	288.0 ± 0.5	284 ± 1	680 ± 90	1.0 ± 0.4
HP+HPT	301.0 ± 0.5	286 ± 2	540 ± 30	5.7 ± 1.0
HP+HPT annealed	300.5 ± 0.5	292 ± 1	720 ± 40	2.1 ± 0.3

[a]The declared uncertainties represent the statistical accuracy (standard deviation) of the experiment and fitting procedure of the sum of exponential components.

https://doi.org/10.1021/acsaem.1c00409
ACS Appl. Energy Mater. 2021, 4, 4831−4844

is the most accurate parameter that can be extracted from the data, and it can be seen from Table 2 that it increases significantly in the HPT process, but subsequent annealing does not produce further changes. This increase is associated with the increase of the intensity of the longer lifetime component τ_2, and as the grain size is reduced by HPT, it is likely that this component represents the excess open volume typically present at the grain boundaries in the polycrystalline system. The shorter lifetime component, likely corresponding to annihilations inside the grains, τ_1, does not change, suggesting that the HPT process does not affect the atomic scale structure of the crystallites. This lifetime of roughly 285 ps is too long to be associated with the "perfect" skutterudite lattice, suggesting that the grains contain high concentrations of vacancy-type defects. Interestingly, the thermal annealing after the HPT-processing decreases the intensity (I_2) of τ_2 and increases somewhat the value of τ_1, even if the average lifetime does not change. It suggests that positron annihilation at grain boundaries is slightly reduced, and that the overall open volume in the vacancy-type defects inside the grains increases. This is likely due to their increasing density, hindering the positron diffusion to the grain boundaries (and hence reducing I_2). It is furthermore in line with the TEM data, showing that the intragrain atomic scale structures (dislocations, clusters of vacancies) evolve in the thermal treatment after HPT.

Long-term stability tests[58] as well as recent studies with a combination of thermal analysis and Knudsen effusion mass spectroscopy prove the structure stability[59] and give confidence for a long-term use at a maximum temperature of 873 K for the HP, BM+HP, BM+HP+HPT, and CP+HPT samples.

3.3. Mechanical Properties. *3.3.1. Hardness.* Static hardness, HV0.1, was measured for the samples s1, s2, and s4 with the results depicted in Figure 14. One should keep in mind that a lower relative density results in lower hardness,[60] while smaller grain sizes, together with a higher defect density, infer higher hardness values. Therefore, these two counteracting variables determine the hardness of the HPT-processed samples. Generally, hardness of all HPT samples was found to be higher than that of the HP sample. After annealing, all samples are a bit harder, obviously related to the slight densification.

Measurements for samples s1 could only be performed in the rim area as the center part was not enough densified and the indenter broke into the surface. Hardness of sample s4 is rather homogeneous with respect to the shear strain and measurements on various spots of the sample did not differ much, exemplarily shown in the inset of Figure 14. The average value of s4 with $HV0.1_{av}$ = 600 (≡ 5.9 GPa) after annealing is lower than that of s1 with $HV0.1_{av}$ = 695 (≡ 6.8 GPa); however, s1 has a higher relative density. For sample s2, with an average relative density of 98.4% and a dislocation density three times higher at the rim than in the center, hardness is governed by grain refinement and the introduction of defects. Thus, hardness strongly increases from the center toward the rim [from HV0.1 = 555 (≡ 5.4 GPa) to HV0.1 = 898 (≡ 8.8 GPa)].

3.3.2. Thermal Expansion. Thermal expansion $\Delta l/l(T)$ was measured for the HP reference sample and for s4= as well as s4||, and the results for the HP sample and exemplarily for s4|| are shown in Figure 15. For the HP sample, all $\Delta l/l(T)$ curves were, within the error bar, alike for the first and second run as well as for increasing and decreasing temperatures, therefore

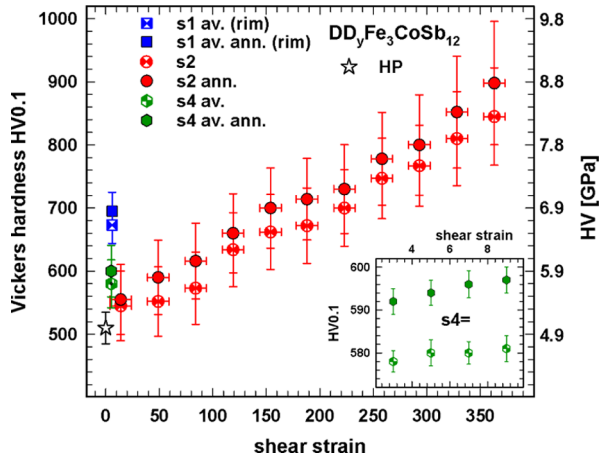

Figure 14. $DD_{0.7}Fe_3CoSb_{12}$: Vickers Hardness, HV01, versus shear strain of samples HP, s1, s2, and s4. Inset: HV01 versus shear strain of s4=.

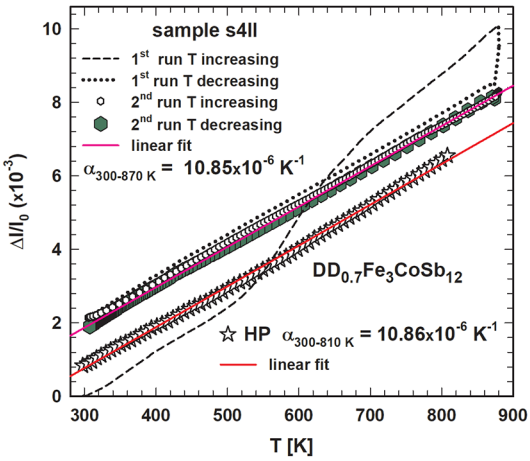

Figure 15. $DD_{0.7}Fe_3CoSb_{12}$: thermal expansion, $\Delta l/l_0$ versus temperature, T, for samples HP and s4||. The solid lines are linear fits.

only one run is shown. The thermal expansion coefficient α follows from a temperature derivative of the length change $\Delta l/l(T)$. For the HP sample, the thermal expansion coefficient is temperature independent above 300 K with $\alpha_{300-810K}$ = 10.86 × 10^{-6} K^{-1}. In contrast to the HP sample, for the HPT samples, s4|| and s4= (shown in Figure S5 in the Supporting Information), at least two heating cycles are needed for a stable behavior. During the first heating, the sample s4|| expands almost in the same way as the HP sample, but at above 600 K, the temperature region where the electrical resistivity shows an anomaly (due to annealing out of defects), the expansion becomes much stronger, however, above about 700 K the curve is again almost parallel to the one of the HP sample. During the first cooling period, sample s4 contracts almost linearly. The second run can already be considered as thermally stable as confirmed by further runs. The thermal expansion coefficient is derived as $\alpha_{300-870K}$ = 10.85 × 10^{-6} K^{-1}, which is in the same order of magnitude as α of the HP sample.

Rietveld refinements of the SXRD data of sample s2C1 and of the CP+HPT (center) sample from our previous work[43] were carried out in order to evaluate the lattice parameter a(T) for each temperature step measured (room temperature to 873 K). The results are plotted in Figure 16. The calculated lattice

https://doi.org/10.1021/acsaem.1c00409
ACS Appl. Energy Mater. 2021, 4, 4831−4844

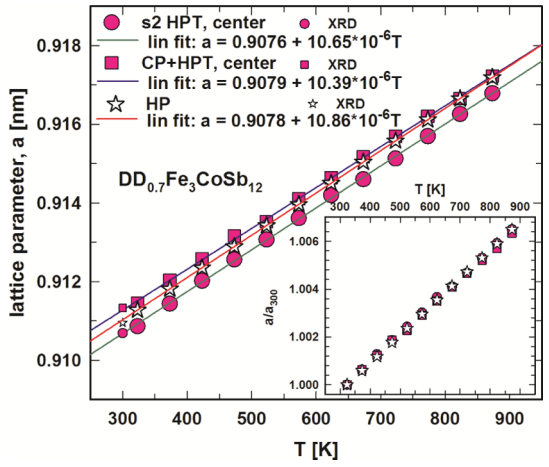

Figure 16. $DD_{0.7}Fe_3CoSb_{12}$: lattice parameter, a, versus temperature, T, for samples s2C, CP+HPT, and HP. Inset: normalized lattice parameter, $a/a_{300\ K}$ versus T.

parameters at room temperature from the XRD spectrum for both samples, s2 and CP+HPT, agree well with the respective synchrotron data. In addition, Figure 16 shows the temperature-dependent lattice parameter data of the HP sample, evaluated from the measured thermal expansion coefficient and the calculated lattice parameter from XRD at room temperature. Generally, all three $a(T)$ graphs increase linearly with increasing temperature, with only minor differences in magnitude. This almost identical behavior is confirmed by the normalized lattice parameters a/a_{300K}, which nearly coincide (Figure 16, inset), revealing upon heating from room temperature to 873 K, an expansion of the lattice by 0.65% for s2 and the HP sample and by 0.63% for the CP +HPT sample. The thermal expansion coefficient could be extracted with average values of $\alpha_{300-870K} = 10.65 \times 10^{-6}\ K^{-1}$ for s2 and $\alpha_{300-870K} = 10.39 \times 10^{-6}\ K^{-1}$ for the CP+HPT sample; both values are slightly lower than the thermal expansion coefficient of the HP sample.

4. CONCLUSIONS

This paper demonstrates that SPD via HPT enables a successful production of bulk samples of p-type skutterudites ($DD_{0.7}Fe_3CoSb_{12}$) with a diameter of 30 mm and thicknesses of 1 mm and 8 mm from commercial raw powder. On these large samples, we studied in detail the influence of shear strain on the structural, physical, and mechanical properties and found in comparison to the HP sample, originating from the same powder, that (i) the grains were refined accompanied by an enhanced defect density, (ii) the relative density was lower, (iii) the shear strain had almost no influence on the Seebeck coefficient, and (iv) the thermal conductivity and the electrical resistivity were strongly strain-dependent. Furthermore, we observed that (v) the enhanced electrical resistivity was overcompensated by a very low thermal conductivity resulting in (vi) ZTs (with one exception, s1) in the range of ZT = 1.3 to almost 1.4 at 823 K for the thin sample and ZT ~ 1.3 for the thick sample, and with (vii) efficiencies of about 14.5% in the temperature range of 423−823 K (except s1 with η = 13.9%). It is important to point out that in all cases, ZT is higher than that of the HP sample (ZT = 1.2 at 823 K).

Although the relative density is reduced, grain refinement enhanced the hardness, which is higher for all HPT samples in comparison to the HP reference sample, with hardness increasing from the center to the rim. The coefficient of thermal expansion for each of the investigated HPT samples is in the same range as the one of the HP reference sample.

Together with the already existing high ZT n-type counterpart,[45,46] this sustainable, energy-saving, cheap, and fast method to produce large p-type bulk skutterudite samples with high ZTs, which are thermally stable, is perfectly suited to directly supply p- and n-legs for TE modules. A further advantage is that it is possible to improve the compatibility and contact problems as well as the recyclability with legs fabricated from the same material family.

■ ASSOCIATED CONTENT

Supporting Information

The Supporting Information is available free of charge at https://pubs.acs.org/doi/10.1021/acsaem.1c00409.

Electrical resistivity, , vs. temperature, T, of samples s2 and s3; Hall resistivity, R_{xy}, vs. magnetic field, H, with least-squares fits; Seebeck coefficient, S(T), vs. temperature, T, of sample s4= and of sample s4||; thermal conductivity, lattice thermal conductivity, λ_{ph}, and electronic part of thermal conductivity, λ_e, vs. temperature, T, of sample s4= and of sample s4||; and thermal expansion, $\Delta l/l_0$, vs. temperature, T, for samples s4= and s4||II (PDF)

■ AUTHOR INFORMATION

Corresponding Author

Gerda Rogl − *Institute of Materials Chemistry, Universität Wien, Wien A-1090, Austria;* orcid.org/0000-0002-8056-5006; Email: gerda.rogl@univie.ac.at

Authors

Oliver Renk − *Erich Schmid Institute of Materials Science, Austrian Academy of Sciences, Leoben A-8700, Austria*

Sanyukta Ghosh − *Thermoelectric Materials and Devices Laboratory, Department of Physics, Indian Institute of Science, Bangalore 560012, India*

Ramesh Chandra Mallik − *Thermoelectric Materials and Devices Laboratory, Department of Physics, Indian Institute of Science, Bangalore 560012, India;* orcid.org/0000-0002-8383-7812

Andriy Grytsiv − *Institute of Materials Chemistry, Universität Wien, Wien A-1090, Austria*

Jiri Bursik − *Institute of Physics of Materials, Czech Academy of Sciences, Brno 61662, Czech Republic*

Erhard Schafler − *Faculty of Physics, Universität Wien, Wien A-1090, Austria*

Filip Tuomisto − *Department of Physics and Helsinki Institute of Physics, University of Helsinki, Helsinki FI-00014, Finland*

Ernst Bauer − *Institute of Solid State Physics, TU Wien, Wien A-1040, Austria*

Peter Franz Rogl − *Institute of Materials Chemistry, Universität Wien, Wien A-1090, Austria;* orcid.org/0000-0002-7733-1612

Complete contact information is available at: https://pubs.acs.org/10.1021/acsaem.1c00409

Notes

The authors declare no competing financial interest.

https://doi.org/10.1021/acsaem.1c00409
ACS Appl. Energy Mater. 2021, 4, 4831−4844

■ ACKNOWLEDGMENTS

The authors thank Treibacher Industries (Dr. M. Hochenhofer) for supplying the skutterudite powder. The authors acknowledge the Indo-Austria joint project WTZ-IN02 funded by DST-BMWF (INT/AUSTRIA/BMWF/P-06/2018) as well as Dr. Y.-C. Chuang from the National Synchrotron Radiation Research Center, Hsinchu, Taiwan and Dr. R. Anbalagan from the Institute of Atomic and Molecular Sciences, Academia Sinica, Taipei City, Taiwan for synchrotron measurements. Thanks are also due to the MEYS, Czech Republic, for support via the bilateral Mobility project 8J21AT015 cosponsored by the Austrian WTZ-CZ16/2021. The authors thank Dr. J. Heikinheimo for the positron annihilation experiments and financial support from the Academy of Finland project nr 315082. The authors thank the Open Access office of the University of Vienna for generous support.

■ REFERENCES

(1) Schierning, G.; Chavez, R.; Schmechel, R.; Balke, B.; Rogl, G.; Rogl, P. Concepts for medium-high to high temperature thermoelectric heat-to-electricity conversion: A review of selected materials and basic considerations of module design. *Transl. Mater. Res.* **2015**, *2*, 025001.

(2) Rogl, G.; Zehetbauer, M. J.; Rogl, P. F. The effect of severe plastic deformation on thermoelectric performance of skutterudites, half-Heuslers and Bi-tellurides. *Mater. Trans.* **2019**, *60*, 2071−2085.

(3) Joshi, G.; Yan, X.; Wang, H.; Liu, W.; Chen, G.; Ren, Z. Enhancement in thermoelectric figure-of-merit of an n-type half-Heusler compound by the nanocomposite approach. *Adv. Energy Mater.* **2011**, *1*, 643−647.

(4) Gelbstein, Y.; Tal, N.; Yarmek, A.; Rosenberg, Y.; Dariel, M. P.; Ouardi, S.; Balke, B.; Felser, C.; Köhne, M. Thermoelectric properties of spark plasma sintered composites based on TiNiSn half-Heusler alloys. *J. Mater. Res.* **2011**, *26*, 1919−1924.

(5) Gürth, M.; Rogl, G.; Romaka, V. V.; Grytsiv, A.; Bauer, E.; Rogl, P. Thermoelectric high ZT half-Heusler alloys $Ti_{1-x-y}Zr_xHf_yNiSn$. *Acta Mater.* **2016**, *104*, 210−222.

(6) Rogl, G.; Sauerschnig, P.; Rykavets, Z.; Romaka, V. V.; Heinrich, P.; Hinterleitner, B.; Grytsiv, A.; Bauer, E.; Rogl, P. (V,Nb)-doped half Heusler alloys based on {Ti,Zr,Hf}NiSn with high ZT. *Acta Mater.* **2017**, *131*, 336−348.

(7) Cohen, I.; Kaller, M.; Komisarchik, G.; Fuks, D.; Gelbstein, Y. Enhancement of the thermoelectric properties of n-type PbTe by Na and Cl co-doping. *J. Mater. Chem. C* **2015**, *3*, 9559−9564.

(8) Guttmann, G. M.; Dadon, D.; Gelbstein, Y. Electronic tuning of the transport properties of off-stoichiometric $Pb_xSn_{1-x}Te$ thermoelectric alloys by Bi_2Te_3 doping. *J. Appl. Phys.* **2015**, *118*, 065102.

(9) Madar, N.; Givon, T.; Mogilyansky, D.; Gelbstein, Y. High thermoelectric potential of Bi_2Te_3 alloyed GeTe- rich phases. *J. Appl. Phys.* **2016**, *120*, 035102.

(10) Gelbstein, Y.; Davidow, J.; Leshem, E.; Pinshow, O.; Moisa, S. Significant lattice thermal conductivity reduction following phase separation of the highly efficient $Ge_xPb_{1-x}Te$ thermoelectric alloys. *Phys. Status Solidi B* **2014**, *251*, 1431−1437.

(11) Khan, S.; Chouhan, M. Review of bismuth telluride (Bi_2Te_3) nanostructured, characterization and properties. *Int. J. Emerg. Tech. in Comp. Sci. and Elec.* **2016**, *21*, 235−238.

(12) Komisarchik, G.; Fuks, D.; Gelbstein, Y. High thermoelectric potential of n-type $Pb_{1-x}Ti_xTe$ alloys. *J. Appl. Phys.* **2016**, *120*, 055104.

(13) Ben-Ayoun, D.; Sadia, Y.; Gelbstein, Y. High temperature thermoelectric properties evolution of $Pb_{1-x}Sn_xTe$ based alloys. *J. Alloys Compd.* **2017**, *722*, 33−38.

(14) Shuai, J.; Sun, Y.; Tan, X.; Mori, T. Manipulating the Ge vacancies and Ge precipitates through Cr doping for realizing the high-performance GeTe thermoelectric material. *Small* **2020**, *16*, 1906921.

(15) Sadia, Y.; Madar, N.; Kaler, I.; Gelbstein, Y. Thermoelectric properties of the quasi-binary $MnSi_{1.73}$-$FeSi_2$ system. *J. Electron. Mater.* **2015**, *44*, 1637.

(16) Meroz, O.; Ben-Ayoun, D.; Beeri, O.; Gelbstein, Y. Development of $Bi_2Te_{2.4}Se_{0.6}$ alloy for thermoelectric power generation applications. *J. Alloys Compd.* **2016**, *679*, 196−201.

(17) Liu, Z.; Mao, J.; Peng, S.; Zhou, B.; Gao, W.; Sui, J.; Pei, Y.; Ren, Z. Tellurium doped n-type Zintl $Zr_3Ni_3Sb_4$ thermoelectric materials: Balance between carrier-scattering mechanism and bipolar effect. *Mater. Today Phys.* **2017**, *2*, 54−61.

(18) Li, H.; Tang, X.; Zhang, Q.; Uher, C. High performance $In_xCe_yCo_4Sb_{12}$ thermoelectric materials with *in situ* forming nanostructured InSb phase. *Appl. Phys. Lett.* **2009**, *94*, 102114.

(19) Xi, L.; Yang, J.; Zhang, W.; Chen, L.; Yang, J. Anomalous dual-element filling in partially filled skutterudites. *J. Am. Chem. Soc.* **2009**, *131*, 5560.

(20) Shi, X.; Yang, J.; Salvador, J. R.; Chi, M.; Cho, J. Y.; Wang, H.; Bai, S.; Yang, J.; Zhang, W.; Chen, L. Multiple-filled skutterudites: High thermoelectric figure of merit through separately optimizing electrical and thermal transports. *J. Am. Chem. Soc.* **2011**, *133*, 7837−7846.

(21) Rogl, G.; Zehetbauer, M.; Kerber, M.; Rogl, P.; Bauer, E. Impact of ball milling and high-pressure torsion on the microstructure and thermoelectric properties of p- and n-type Sb-based skutterudites. *Mater. Sci. Forum* **2011**, *667*, 1089−1094.

(22) Ballikaya, S.; Uher, C. Enhanced thermoelectric performance of optimized Ba, Yb filled and Fe substituted skutterudite compounds. *J. Alloys Compd.* **2014**, *585*, 168−172.

(23) Rogl, G.; Grytsiv, A.; Rogl, P.; Peranio, N.; Bauer, E.; Zehetbauer, M.; Eibl, O. n-type skutterudites $(R,Ba,Yb)_yCo_4Sb_{12}$ (R = Sr, La, Mm, DD, SrMm, SrDD) approaching ZT∼2.0. *Acta Mater.* **2014**, *63*, 30−43.

(24) Rogl, G.; Grytsiv, A.; Yubuta, K.; Puchegger, S.; Bauer, E.; Raju, C.; Mallik, R. C.; Rogl, P. In-doped multifilled n-type skutterudites with ZT= 1.8. *Acta Mater.* **2015**, *95*, 201−211.

(25) Guo, L.; Xu, X.; Salvador, J. R. Ultrafast carriers dynamics in filled-skutterudites. *Appl. Phys. Lett.* **2015**, *106*, 231902.

(26) Rogl, G.; Grytsiv, A.; Heinrich, P.; Bauer, E.; Kumar, P.; Peranio, N.; Eibl, O.; Horky, J.; Zehetbauer, M.; Rogl, P. New bulk p-type skutterudites $DD_{0.7}Fe_{2.7}Co_{1.3}Sb_{12-x}X_x$ (X = Ge, Sn) reaching ZT>1.3. *Acta Mater.* **2015**, *91*, 227−238.

(27) Duan, B.; Yang, J.; Salvador, J. R.; He, Y.; Zhao, B.; Wang, S.; Wei, P.; Ohuchi, F. S.; Zhang, W.; Hermann, R. P.; Gourdon, O.; Mao, S. X.; Cheng, Y.; Wang, C.; Liu, J.; Zhai, P.; Tang, X.; Zhang, Q.; Yang, J. Electronegative guests in $CoSb_3$. *Energy Environ. Sci.* **2016**, *9*, 2090.

(28) Wang, S.; Salvador, J. R.; Yang, J.; Wei, P.; Duan, B.; Yang, J. High-performance n-type $Yb_xCo_4Sb_{12}$: From partially filled skutterudites towards composite thermoelectrics. *NPG Asia Mater.* **2016**, *8*, No. e285.

(29) Snyder, G. J.; Toberer, E. S. Complex thermoelectric materials. *Nat. Mater.* **2008**, *7*, 105−114.

(30) Kim, S. I.; Lee, K. H.; Mun, H. A.; Kim, H. S.; Hwang, S. W.; Roh, J. W.; Yang, D. J.; Shin, W. H.; Li, X. S.; Lee, Y. H.; Snyder, G. J.; Kim, S. W. Dense dislocation arrays embedded in grain boundaries for high-performance bulk thermoelectrics. *Science* **2015**, *348*, 109−114.

(31) Zhang, Q.; Zhou, Z.; Dylla, M.; Agne, M. T.; Pei, Y.; Wang, L.; Tang, Y.; Liao, J.; Li, J.; Bai, S.; Jiang, W.; Chen, L.; Jeffrey Snyder, G. Realizing high-performance thermoelectric power generation through grain boundary engineering of skutterudite-based nanocomposites. *Nano Energy* **2017**, *41*, 501−510.

(32) Rogl, G.; Rogl, P. Skutterudites: Progress and Challenges. In *Novel Thermoelectric Materials and Device Design Concepts*; Skipidarov, S., Nikitin, M., Eds.; Springer, 2019; Vol. *1*(9), pp 177−203.

(33) Ivanisenko, Yu.; Kulagin, R.; Fedorov, V.; Mazilkin, A.; Scherer, T.; Baretzky, B.; Hahn, H. High pressure torsion extrusion as a new severe plastic deformation process. *Mater. Sci. Eng., A* **2016**, *664*, 247−256.

https://doi.org/10.1021/acsaem.1c00409
ACS Appl. Energy Mater. 2021, 4, 4831−4844

(34) Rogl, G.; Zehetbauer, M. J.; Rogl, P. F. The effect of severe plastic deformation on thermoelectric performance of skutterudites, half-Heuslers and Bi-tellurides. *Mater. Trans.* **2019**, *60*, 2071−2085.
(35) Mallik, R. C.; Anbalagan, R.; Rogl, G.; Royanian, E.; Heinrich, P.; Bauer, E.; Rogl, P.; Suwas, S. Thermoelectric properties of $Fe_{0.2}Co_{3.8}Sb_{12-x}Te_x$ skutterudites. *Acta Mater.* **2013**, *61*, 6698−6711.
(36) Anbalagan, R.; Rogl, G.; Zehetbauer, M.; Sharma, A.; Rogl, P.; Suwas, S.; Mallik, R. C. Effect of high-pressure torsion on texture, microstructure, and Raman spectroscopy: Case study of Fe- and Te-substituted $CoSb_3$. *J. Electron. Mater.* **2014**, *43*, 3817−3823.
(37) Zhang, L.; Grytsiv, A.; Bonarski, B.; Kerber, M.; Setman, D.; Schafler, E.; Rogl, P.; Bauer, E.; Hilscher, G.; Zehetbauer, M. Impact of high-pressure torsion on the microstructure and physical properties of $Pr_{0.67}Fe_3CoSb_{12}$, $Pr_{0.71}Fe_{3.5}Ni_{0.5}Sb_{12}$, and $Ba_{0.06}Co_4Sb_{12}$. *J. Alloys Compd.* **2010**, *494*, 78−83.
(38) Rogl, G.; Aabdin, Z.; Schafler, E.; Horky, J.; Setman, D.; Zehetbauer, M.; Kriegisch, M.; Eibl, O.; Grytsiv, A.; Bauer, E.; Reinecker, M.; Schranz, W.; Rogl, P. Effect of HPT processing on the structure, thermoelectric and mechanical properties of $Sr_{0.07}Ba_{0.07}Yb_{0.07}Co_4Sb_{12}$. *J. Alloys Compd.* **2012**, *537*, 183−189.
(39) Rogl, G.; Rogl, P.; Bauer, E.; Zehetbauer, M. Severe Plastic Deformation, a Tool to Enhance Thermoelectric Performance. In *Thermoelectric Nanomaterials*; Kuomoto, K., Mori, T., Eds.; Springer Series in Materials Science; Springer, 2013; Vol. *182*; pp 193−254.
(40) Rogl, G.; Grytsiv, A.; Bursik, J.; Horky, J.; Anbalagan, R.; Bauer, E.; Mallik, R. C.; Rogl, P.; Zehetbauer, M. Changes in microstructure and physical properties of skutterudites after severe plastic deformation. *Phys. Chem. Chem. Phys.* **2015**, *17*, 3715−3722.
(41) Rogl, G.; Grytsiv, A.; Rogl, P.; Royanian, E.; Bauer, E.; Horky, J.; Setman, D.; Schafler, E.; Zehetbauer, M. Dependence of thermoelectric behavior on severe plastic deformation parameters: A case study on p-type skutterudite $DD_{0.60}Fe_3CoSb_{12}$. *Acta Mater.* **2013**, *61*, 6778−6789.
(42) Rogl, G.; Grytsiv, A.; Rogl, P.; Bauer, E.; Hochenhofer, M.; Anbalagan, R.; Mallik, R. C.; Schafler, E. Nanostructuring of p- and n-type skutterudites reaching figures of merit of approximately 1.3 and 1.6, respectively. *Acta Mater.* **2014**, *76*, 434−448.
(43) Rogl, G.; Grytsiv, A.; Anbalagan, R.; Bursik, J.; Kerber, M.; Schafler, E.; Zehetbauer, M.; Bauer, E.; Rogl, P. Direct SPD-processing to achieve high-ZT skutterudites. *Acta Mater.* **2018**, *159*, 352−363.
(44) Rogl, G.; Yubuta, K.; Kerber, M.; Grytsiv, A.; Zehetbauer, M.; Bauer, E.; Rogl, P. Sustainable and simple processing technique for n-type skutterudites with high ZT and their analysis. *Acta Mater.* **2019**, *173*, 9−19.
(45) Rogl, G.; Ghosh, S.; Renk, O.; Yubuta, K.; Grytsiv, A.; Schafler, E.; Zehetbauer, M.; Mallik, R. C.; Bauer, E.; Rogl, P. Influence of shear strain on HPT-processed n-type skutterudites yielding ZT=2.1. *J. Alloys Compd.* **2021**, *855*, 157409.
(46) Rogl, G.; Ghosh, S.; Renk, O.; Yubuta, K.; Grytsiv, A.; Schafler, E.; Zehetbauer, M.; Mallik, R. C.; Bauer, E.; Rogl, P. HPT production of large bulk skutterudites. *J. Alloys Compd.* **2021**, *854*, 156678.
(47) Wacha, W. An integrated software system for X-ray powder analysis,. Diploma Thesis, University of Technology, Vienna, Austria, 1989.
(48) Rodriguez-Carvajal, J. J. *FULLPROF, Abstract of the Satellite Meeting on Powder Diffraction of the XV Congress*; Int. Union of Crystallography: Talence, France, 1990; p 127.
(49) Ungar, T.; Schafler, E.; Gubicza, J. Microstructure of bulk nanomaterials determined by X-Ray line profile analysis. In *Bulk Nanostructured Materials*; Zehetbauer, M. J., Zhu, Y. T., Eds.; VCH Wiley: New York, 2009.
(50) Ribárik, G.; Gubicza, J.; Ungár, T. Correlation between strength and microstructure of ball-milled Al-Mg alloys determined by X-ray diffraction. *J. Mater. Sci. Eng. A* **2004**, *387*−*389*, 343.
(51) Schafler, E. Strength response upon pressure release after high pressure torsion deformation. *Scr. Mater.* **2011**, *64*, 130−132.
(52) Lohmiller, J.; Baumbusch, R.; Kerber, M. B.; Castrup, A.; Hahn, H.; Schafler, E.; Zehetbauer, M.; Kraft, O.; Gruber, P. A. Following the deformation behavior of nanocrystalline Pd films on polyimide substrates using in situ synchrotron XRD. *Mech. Mater.* **2013**, *67*, 65−73.
(53) Tuomisto, F.; Makkonen, I. Defect identification in semiconductors with positron annihilation: Experiment and theory. *Rev. Mod. Phys.* **2013**, *85*, 1583−1631.
(54) Kim, H.-S.; Gibbs, Z. M.; Tang, Y.; Wang, H.; Snyder, G. J. Characterization of Lorenz number with Seebeck coefficient measurement. *APL Mater.* **2015**, *3*, 041506.
(55) Rogl, G.; Setman, D.; Schafler, E.; Horky, J.; Kerber, M.; Zehetbauer, M.; Falmbigl, M.; Rogl, P.; Royanian, E.; Bauer, E. High-pressure torsion, a new processing route for thermoelectrics of high ZTs by means of severe plastic deformation. *Acta Mater.* **2012**, *60*, 2146−2157.
(56) Rogl, G.; Soprunyuk, V.; Schranz, W.; Zehetbauer, M. J.; Bursik, J.; Müller, H.; Bauer, E.; Rogl, P. F. Resistivity and thermal expansion (4.2-820 K) of skutterudites after severe plastic deformation via HPT. *Z. Anorg. Allg. Chem.* **2020**, *646*, 1267−1272.
(57) Goldsmid, H. J.; Sharp, J. W. Estimation of the thermal band gap of a semiconductor from Seebeck measurements. *J. Electron. Mater.* **1999**, *28*, 869−872.
(58) Rogl, G.; Grytsiv, A.; Bauer, E.; Rogl, P. Thermoelectric Sb-based skutterudites for medium temperatures. *Advanced Thermoelectrics*; Ren, Z., Lan, Y., Zhang, Q., Eds.; CRC Press: Boca Raton, FL, 2019; Vol. *5*; pp 195−231.
(59) Zelenka, F.; Brož, P.; Vřešťál, J.; Buršík, J.; Rogl, G.; Grytsiv, A.; Rogl, P. Study of thermal stability of p-type skutterudites $DD_{0.7}Fe_3CoSb_{12}$ by Knudsen effusion mass spectrometry. *RSC Adv.* **2019**, *9*, 21451−21459.
(60) Rogl, G.; Rogl, P. Mechanical properties of skutterudites. *Sci. Adv. Mater.* **2011**, *3*, 517−538.

https://doi.org/10.1021/acsaem.1c00409
ACS Appl. Energy Mater. 2021, 4, 4831−4844